

Microstructural Evolution and Mechanical Properties of Direct Metal Laser-Sintered (DMLS) CoCrMo After Heat Treatment



KAUSTUBH KRISHNA BAWANE, DHEEPA SRINIVASAN,
and DIPANKAR BANERJEE

Microstructures and tensile properties of Direct Metal Laser-Sintered (DMLS) CoCrMo were investigated in the as-printed condition and after heat treatment. A dense (> 99.5 pct) as-printed DMLS CoCrMo was obtained in the as-printed condition eliminating the need for any hot isostatic pressing. Solution heat treatment carried out at 1150 °C revealed complete recrystallization resulting in an equiaxed grain structure with an average grain size of 40 μm . The microstructure after solution heat treatment and aging at 980 °C revealed inter and intragranular precipitations, enriched in Mo and Si. Solution treatment resulted in the decrease of the room-temperature tensile strength from 1378 MPa (as-printed) to 1114 MPa, which was attributed to the increasing grain size from 0.6 to 1 μm (column width) to ~ 40 μm (grain size). The decrease in yield strength was accompanied by the increasing ductility from 5.7 to 15 pct. An enhancement in ductility to nearly 25 pct was observed in tensile tests at 925 °C. This paper comprises a detailed microstructural evaluation of DMLS CoCrMo alloy to determine its suitability for high-temperature structural applications involving repair and refurbishment of components, including an evaluation of microstructural and tensile properties after welding the DMLS CoCrMo to cast FSX414.

<https://doi.org/10.1007/s11661-018-4771-4>

© The Minerals, Metals & Materials Society and ASM International 2018

I. INTRODUCTION

ADDITIVE manufacturing *via* the direct metal laser-sintered (DMLS) process is gaining popularity in various sectors of structural engineering components as an economic approach to fabricating very expensive hardware made of high-temperature alloys. The key advantage of using the 3D printing approach is in its ability to compress the design cycle and reduce part development time by over 70 to 80 pct, compared with the current processes.^[1] In addition, additive manufacturing paves the way for new engineering capability to optimize part and system designs in a way that cannot be achieved with the traditional manufacturing processes. Thus, the reduced part counts, minimized inventory, increases in the first pass yield, the improved design of parts, systems, and shapes once thought impossible to

make, thereby enabling realization of products that are lighter, stronger, and more efficient, are all potential revolutionary advantages in design to manufacturing stages.^[1–9] As a consequence, there has been extensive research on the DMLS process directed toward optimizing processing parameters and developing structure–property correlations in various structural alloys.^[10–19] The process parameters in this study were developed to ensure a nearly dense microstructure with little porosity, details of which can be found in Reference 30.

Cobalt-based alloys are widely used in applications that encounter high temperature, oxidation, and hot corrosion, such as nuclear power plants, automobile engines, aerospace fuel nozzle, engine vanes, and biomedical implants.^[20] Prior study on DMLS CoCrMo alloys mainly deals with biomedical applications rather than engineering applications.^[21–30] There are limited reports on DMLS CoCrMo for structural applications, especially those that involve weldability of the DMLS alloys. The objectives of the present study were three-fold: (a) to evaluate the characteristics of the as-printed DMLS CoCrMo alloy built through an optimized process that eliminates HIP (hot isostatic pressing), (b) to evaluate the effects of solution treatment and aging on the microstructural and tensile properties of DMLS

KAUSTUBH KRISHNA BAWANE and DIPANKAR BANERJEE are with the Department of Materials Engineering, Indian Institute of Science, Bangalore, India. Contact e-mail: dbanerjee@iisc.ac.in DHEEPA SRINIVASAN is with GE Power, GE India Industrial Pvt. Ltd., Bangalore, India. Contact e-mail: dheepasrinivasan6@gmail.com

Manuscript submitted March 26, 2018.

Table I. Nominal Chemical Compositions of Alloys Used in This Study

Alloy	C	Si	Cr	Mo	Ni	Mn	Zr	Ta	W	Co
CoCrMo	0.1	0.88	28.77	7	—	0.82	—	—	—	bal.
Filler Wire	0.05	—	29	—	20	—	0.01	7	—	bal.
FSX-414 [5]	0.2 to 0.3	0.5 to 1.0	28.5 to 30.5	—	9.5 to 11.5	0.4 to 1.0	—	—	6.5 to 7.5	bal.

Table II. DMLS CoCrMo Process Parameters

Material	CoCrMo
Laser Power	290 W
Laser Beam Diameter	80 μm
Layer Thickness	40 μm
Shielding Gas	nitrogen
Hatch Distance	110 μm
Scanning Speed	950 mm/s
Powder Size	10 to 50 μm
Powder Source	EOS

CoCrMo, and (c) to evaluate the feasibility of welding the DMLS CoCrMo to cast FSX414 (a solid solution-strengthened Co-based alloy extensively used in gas turbine hardware), using Co-based Nozzalloy™ filler wire in order to simulate the repair and refurbishment of the cast FSX414 components.

II. EXPERIMENTAL DETAILS

Table I lists the nominal compositions of the alloys used in this study. The alloys include the DMLS CoCrMo (powders), the cast FSX414 components, and the weld filler wire compositions. A flat coupon of dimensions 125 mm (length) \times 43 mm (width) \times 10 mm (thickness) was printed using an EOS 280 machine at INTECH-DMLS, Bangalore, India, using the nominal parameters listed in Table II. Cylindrical DMLS CoCrMo coupons (length of 95 mm, dia. of 15 mm) were also built under identical conditions in the same build plate to prepare tensile dog-bone specimens. The powders used were procured from EOS, GmbH, with sizes between 5 and 45 μm and were analyzed using a particle size analyzer, Mastersizer 2000E, a laser diffraction-based powder size analyzer. SEM-EDS analysis was performed on Zeiss EVO18 Scanning Electron Microscope (SEM) along with Oxford link energy-dispersive spectroscopy (EDS) to characterize the morphology and composition of the powders. Preliminary phase identification was carried out using X-ray diffraction on the powders on a Rigaku Miniflex600 (Cr K_{α} with 2.29 Å wavelength). The printed samples were evaluated for their porosity and microstructure transverse to the build direction, across various spans of the coupon, as shown in the schematic in Figure 1(a). Porosity was evaluated using Nikon Optical Microscope (Eclipse MA200) and Clemex Image analysis software. Microstructures were evaluated after etching (using

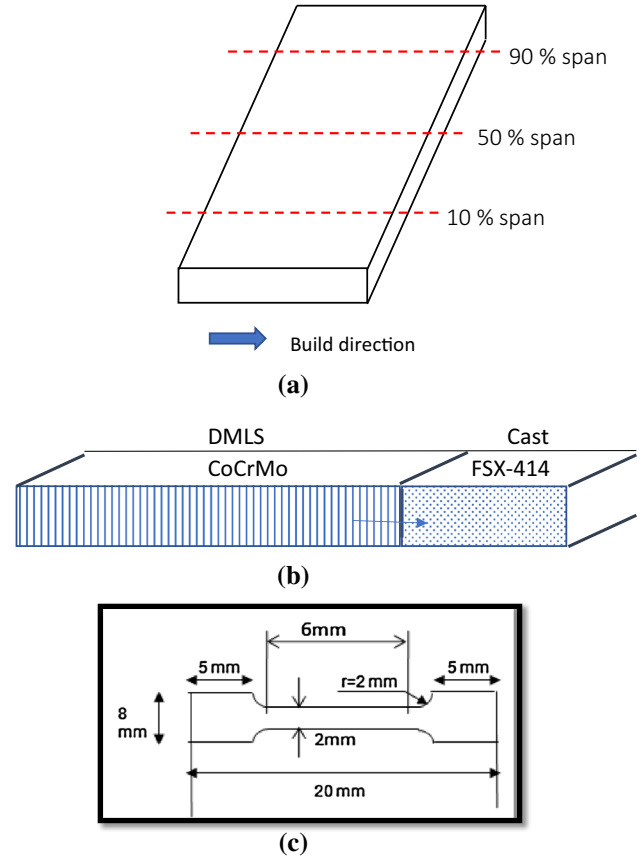


Fig. 1—(a) Schematic of the DMLS CoCrMo coupon, (b) DMLS CoCrMo welded to cast FSX414, and (c) specimen geometry.

5 pct HCl (Electrolytic, 6 V) for 10 seconds). Porosity and grain size measurements and distribution were carried out using ImageJ software. The as-printed samples were subjected to solution heat treatments at 1150 °C for 1.5 hours in vacuum, followed by aging heat treatment for 2.5 hours at 980 °C. This is the heat treatment given to FSX414 superalloy as part of the solution and aging protocol, and the DMLS CoCrMo was given the same heat treatment. There was no stress-relieving heat treatment given to remove the sample coupons from the build plate as is normally done for DMLS samples. Detailed microstructural analyses of the samples were carried out using a Zeiss Sigma, Field emission gun, SEM. Transmission Electron Microscopy (TEM) was carried out on a FEI Technai F30 to identify the phases present in the as-printed samples. Electron-transparent samples were made using the Twin jet electropolisher (80:20: methanol:perchloric

acid, 5 V, 20 mA). Electron backscattered diffraction (EBSD) analysis was performed, using the HKL EBSD link system attached to the Zeiss EVO18 SEM to determine texture evolution during 3D printing as well as texture changes after the heat treatment. Vickers microhardness measurement was carried out using a Shimadzu microhardness tester, using 300 g loads. Tensile testing was carried out at the room temperature and at 925 °C on the as-printed and heat-treated DMLS CoCrMo samples. Residual stresses were measured on the as-printed DMLS coupons using a Rigaku Automate II micro-area X-ray residual stress, *via* the $\text{Sin}^2\Psi$ technique. The surface was electropolished to reduce surface roughness, and measurements were carried out along various locations of the as-printed coupon along the build, starting from position close to the base. Residual stress measurement was carried out using (220) diffraction peak of FCC Cobalt with a Chromium K_α source (wavelength-2.29 Å).

The DMLS CoCrMo coupon was welded to a cast FSX414 (Cobalt-based superalloy) using a Nozzalloy weld filler wire (~ 1 mm thick) *via* a conventional TIG

(tungsten inert gas welding) technique, as shown in the schematic in Figure 1(b). This was subjected to a postweld heat treatment (1150 °C, 1.5 hours in vacuum), and the microstructural and mechanical properties were evaluated across the weldment (arrowed in Figure 1(b)). Owing to the geometry of the joint, flat micro-tensile specimens were extracted transverse to the weldment as shown in Figure 1(c), with dimensions (6 mm gage length, 2 mm width, and 0.5 mm thickness). All tests were carried out at a strain rate of 0.05 mm/mm.

III. RESULTS

A. Microstructure: The As-Printed DMLS CoCrMo

The SEM of the EOS CoCrMo powder (Figure 2(a)) reveals a spherical morphology with particle size in the range of 5 to 55 μm , with an average of 25 μm , as shown in Figure 2(b). The process parameters were optimized to obtain a dense microstructure in the as-printed condition, as shown in the representative optical

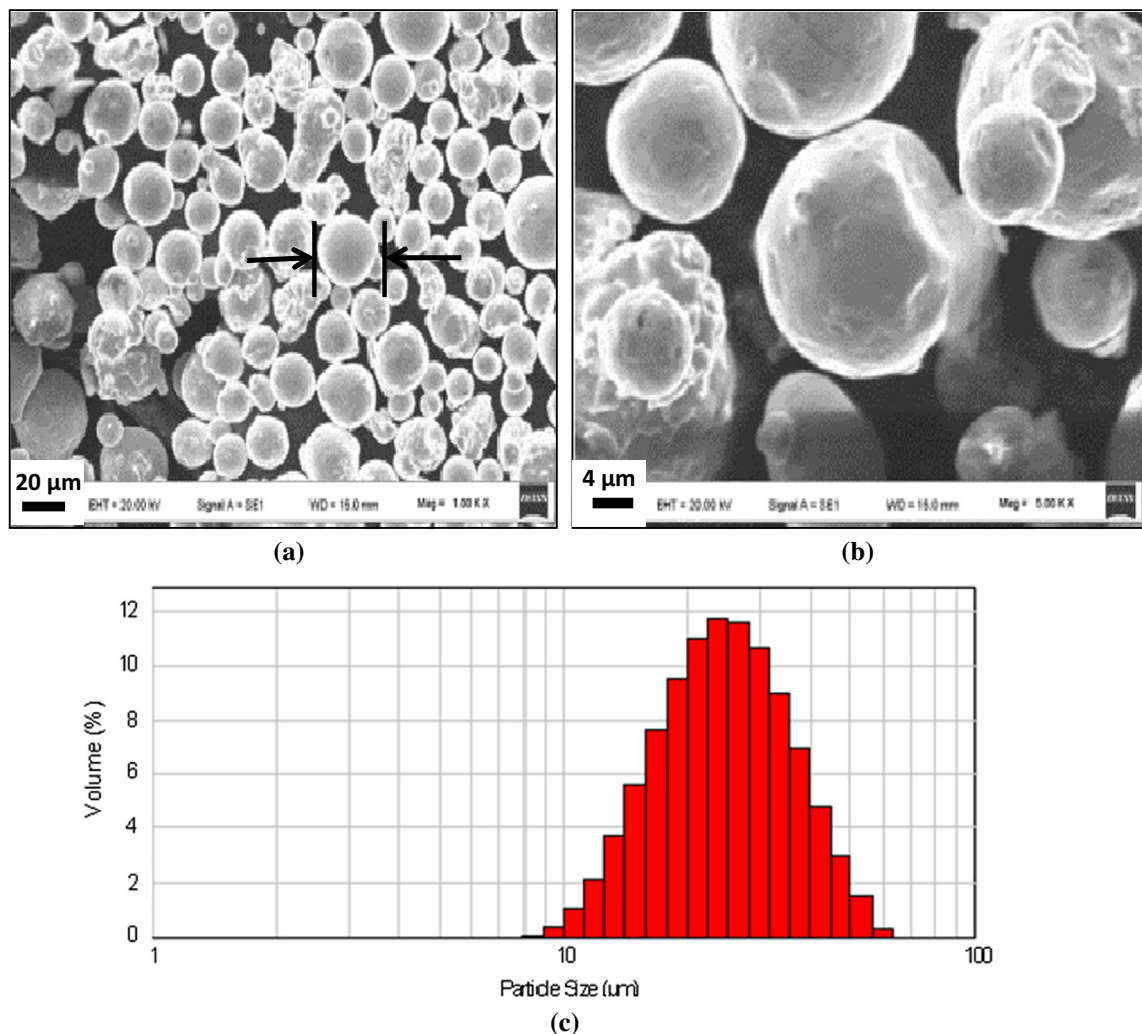


Fig. 2—SEM images showing size and morphology of the as-received CoCrMo powders at (a) low magnification, (b) high magnification, and (c) powder size distribution.

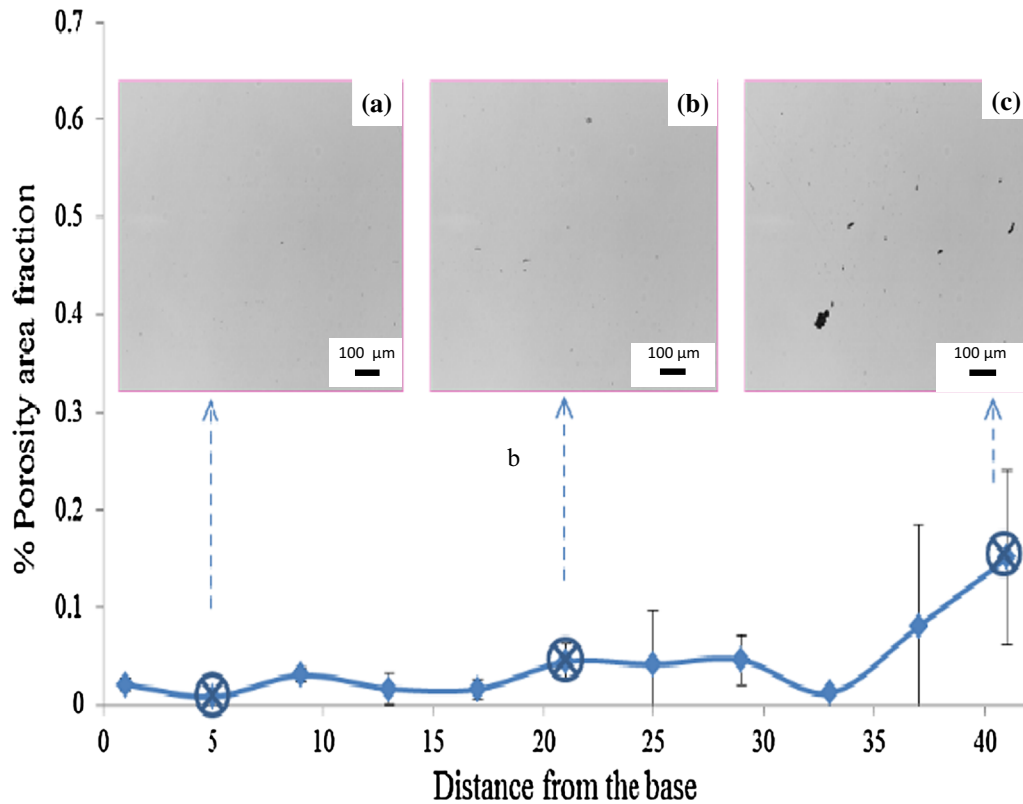


Fig. 3—Porosity distribution on transverse section of the as-printed DMLS CoCrMo along the build direction at three locations, at a distance of, (a) 5 mm, (b) 20 mm and (c) 40 mm, from the base.

micrographs in Figures 3(a) and (b), in the unetched condition. The average porosity was around 0.043 ± 0.04 pct, with little or no variation in the distribution along the build direction. Most of the fine pores have a spherical morphology with sporadic occurrence of some irregular morphology. Interlayer porosity, which is commonly present in DMLS-processed alloys in the as-printed condition, was not observed, and a dense coupon was obtained requiring no subsequent HIP (hot isostatic pressing). Figures 4(a) through (e) show representative optical micrographs of the as-printed DMLS CoCrMo after etching. The optical micrographs of the transverse section (transverse to the build direction) in Figure 4(a) reveal the occurrence of a few irregular pores in the vicinity of the melt pool boundary along with sporadic microcracks as shown in Figures 4(b) and (c). It can be seen that microcracks are almost always perpendicular to the melt pool boundary. The size of the weld pool is around $\sim 120 \mu\text{m}$ wide and $\sim 60 \mu\text{m}$, as shown in the macrostructure in Figure 4(d), which clearly shows solidified melt pools stacked layer by layer. Figure 4(d) shows a collage of the printed macrostructure of the as-printed DMLS CoCrMo, starting with the base layer (the first layer to be printed). Solidified scan paths can be seen in the base macrostructure (Figure 4(e)), revealing the angle between the two scan paths/weld pools, as 67 deg, reflective of the actual printing process. Figures 5(a) through (d) show SEM micrographs of

the as-printed DMLS CoCrMo. A columnar structure was seen inside the solidified melt pool (Figure 5(a)). Figure 5(b) shows that the columnar structures can extend across the melt pool boundaries. Thus, dendritic columns growing inside melt pool during solidification seem to be adopting orientation of columns in previous layers and similarly oriented columns tend to form domains inside the melt pool, as revealed in Figures 5(a) through (c). Backscattered electron images (Figures 5(d) through (f)) reveal the primary dendrite arm spacing (PDAS) to be of 600 to 1000 nm. No branching into secondary dendritic arms was observed throughout the coupon. Unetched BSE images (Figures 5(e) and (f)) show the presence of elongated bright precipitates in the interdendritic regions as well as plate-like features that run across the columns at different angles.

In order to further discern location, size, morphology and composition of various phases, transmission electron microscopy was carried out. Figure 6(a) shows TEM bright field image of the intradendritic region of the sample at [011] zone axis. Dark plate like phases were present at an angle of 70.52° as shown in Figure 6(b). Fringe contrast can also be observed. High resolution (HR) TEM image and corresponding fast Fourier transform (FFT) pattern revealed fully coherent alternate bands of ϵ -HCP and γ -FCC phase in the region of dark plate phase (as shown in Figures 6(b) and (c)). The width of the ϵ -HCP band is ~ 9 nm. Figure 6(d) shows an FFT pattern of entire HRTEM image

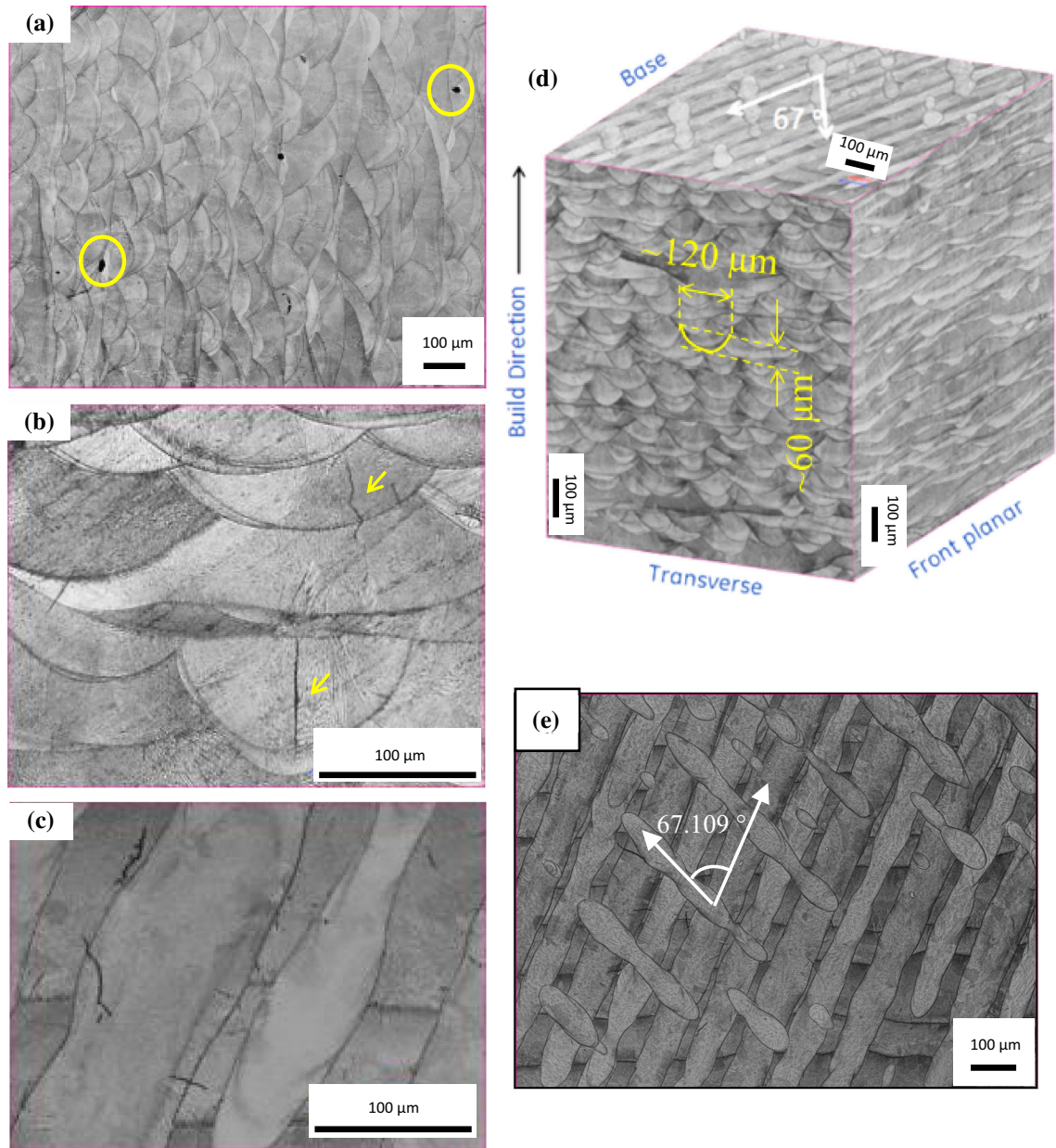


Fig. 4—Optical micrographs of transverse section of the as-printed DMLS CoCrMo at (a) low magnification showing irregular pores at the interlayer boundaries; (b, c) high magnification showing microcracks; (d) micrographs with a collage of transverse, front planar, and base sections of the as-printed DMLS CoCrMo; (e) the base layer orientation.

revealing the following orientation relationship (OR): $(11\bar{1})_{\gamma} \parallel (000\bar{1})_{\varepsilon}$, $[011]_{\gamma} \parallel [\bar{1}2\bar{1}0]_{\varepsilon}$, namely, a Shoji-Nishiyama orientation relationship between γ -FCC and ε -HCP phases. High Angle-Annular Dark Field (HAADF) STEM images in Figure 6(e) shows precipitates with elongated and globular morphology in the interdendritic region similar to the BSE image. Dark globular precipitates (~ 20 to 70 nm in diameter) are seen (arrowed) along with bright disc shaped precipitates (circled) (~ 30 to 70 nm) in the matrix. Bright and dark contrast of elongated and globular precipitates arose as a result of elemental segregation in the

interdendritic region. TEM-EDS analysis revealed the chemical compositions of the bright disc shaped precipitates to be rich in Mo and Si, while globular dark precipitates were enriched in Si, as shown in Table III.

B. Microstructures—Solution-Treated and Aged DMLS CoCrMo

Figure 7(a) shows optical micrographs of solution-treated DMLS CoCrMo and its corresponding grain size distribution in Figure 7(b) indicating an

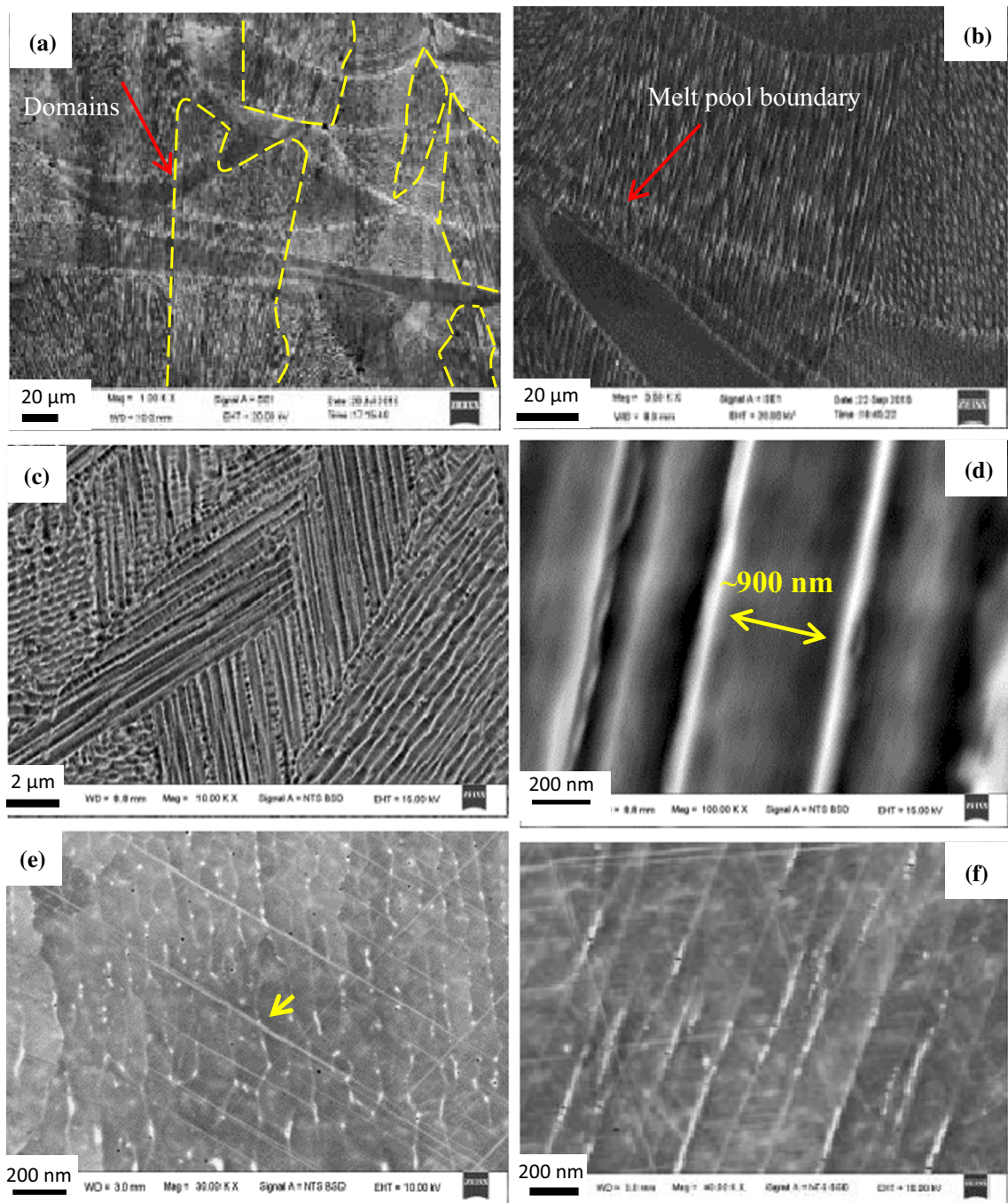


Fig. 5—Scanning electron micrographs of the as-printed DMLS CoCrMo (a) showing a columnar microstructure and domains (grains); (b) a one-to-one matching along the melt pool boundary, in the unetched condition; (c, d) backscattered electron images, at low and high magnifications showing a bright contrast in the interdendritic region; (e, f) high-magnification BSE images showing interdendritic precipitates and ϵ -HCP (arrow) cutting across the columns, in the unetched condition.

average grain size of $45 \mu\text{m}$. Figure 7(c) is a representative collage from the transverse and longitudinal (along the build direction) sections of solution heat-treated DMLS CoCrMo. The grain size ranges between 5 and $100 \mu\text{m}$ and shows no correlation with either powder size or melt pool size but may be related to the columnar domains. While the melt pool boundaries cannot be detected after heat treatment, the remnants of

the columnar dendritic structure are present as a network of precipitates in bright contrast within the grains, as seen in Figures 7(e) and (f). BSE images of the solution-treated samples in Figure 7(e) show twinning in the equiaxed microstructure. High-magnification BSE images of unetched solution-treated samples in Figures 7(e) and (f) show the elliptical-shaped bright precipitates on the grain boundaries very similar to

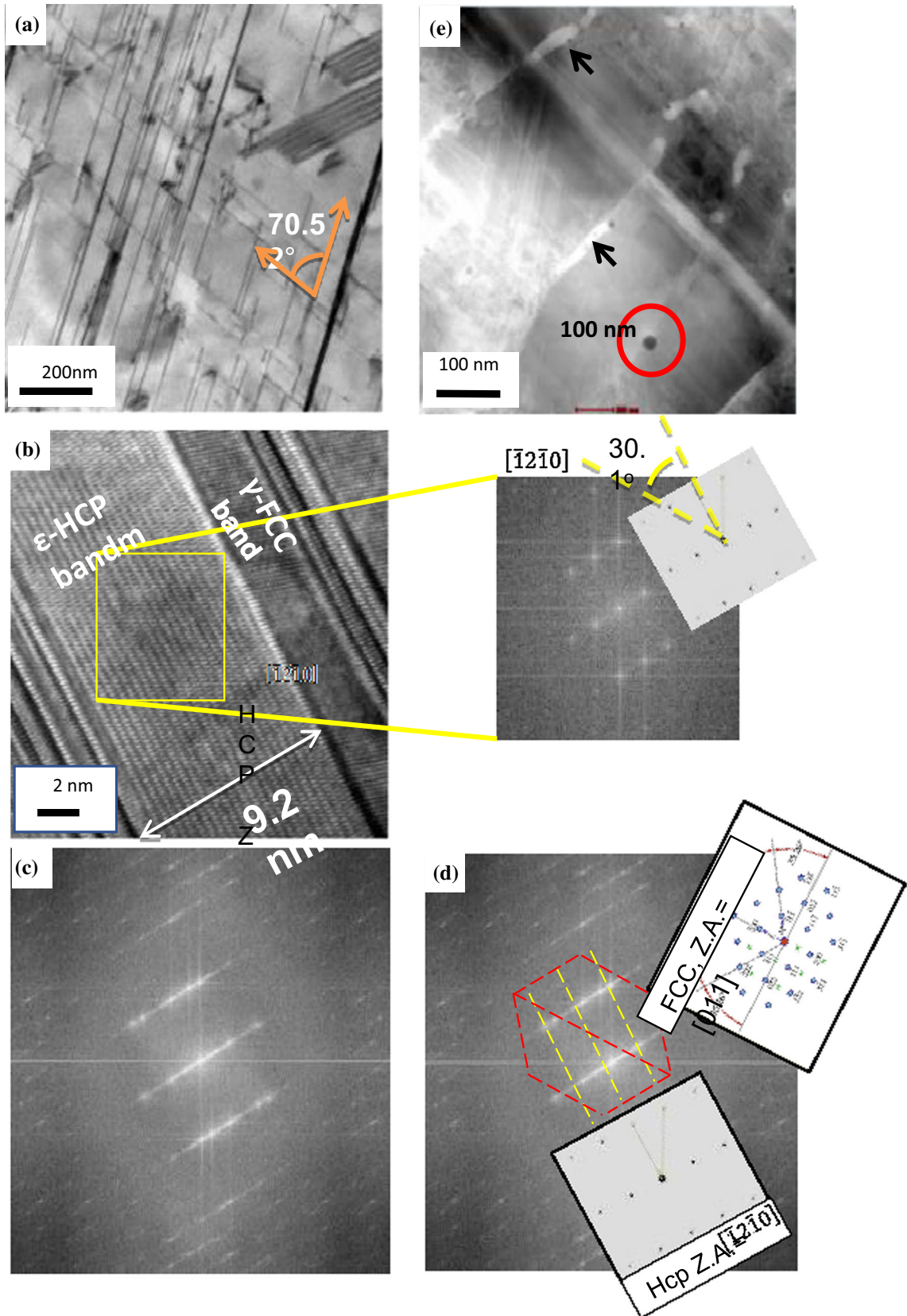


Fig. 6—(a) TEM brightfield images of the as-printed DMLS CoCrMo sample showing ϵ -HCP phases in γ -FCC CoCrMo matrix. (b) High-resolution (HR) TEM image of the as-printed DMLS CoCrMo and its corresponding FFT pattern showing the existence of HCP phase, (c, d) FFT pattern showing reflections belonging to both FCC and HCP phases and their orientation relationship, (e) High Angle Annular Dark Field (HAADF) STEM images showing elongated bright precipitates and globular black precipitates in the interdendritic region.

Table III. Chemical Analysis of Various Phases in the As-Printed DMLS CoCrMo Specimen Using TEM-EDS

Elements		Co	Cr	Mo	Mn	Si
Bright Precipitate	wt pct	44.2	27.4	22.3	2.7	3.3
	at. pct	44.7	31.4	13.0	3.0	7.0
Dark Precipitate	wt pct	55.1	28.4	7.6	3.0	5.8
	at. pct	51.2	30.0	4.4	3.1	11.3
Matrix	wt pct	60.4	26.4	7.4	3.0	1.8
	at. pct	58.4	29.1	4.5	3.9	3.7

those observed as elongated bright precipitates in the as-printed DMLS CoCrMo (Figure 6(e)). Dark globular phases can also be seen, especially along the grain boundaries (Figure 7(e), arrowed). The solution-treated CoCrMo was subjected to an aging heat treatment to evaluate the high-temperature stability. Figure 8(a) shows a representative optical micrograph of the aged DMLS CoCrMo sample having equiaxed grains with similar grain size as that of the solution heat-treated samples. Precipitations of various phases inside grains and along the grain boundaries can be seen after aging, as shown in the BSE images in Figures 8(b) and (c). The dark precipitates have globular morphology similar to those observed in the as-printed and solution heat-treated specimens. Most of the intragranular bright precipitates have a plate morphology, while some are globular. Almost all the intergranular bright precipitates have either globular or elliptical morphology similar to the intergranular precipitates in the solution-treated samples. The entire grain boundary is decorated with these precipitates on aging. SEM-EDS elemental analysis results of the precipitates are presented in Table IV which compares the chemical compositions of the matrix and both the bright and dark precipitates. The bright precipitates are rich in molybdenum and silicon, while the dark phase is rich in silicon and manganese. There was no significant difference between plate-shaped and globular bright precipitates, with respect to the chemistry, and both the bright precipitates are rich in molybdenum and silicon. ϵ -HCP Co is present in the solution-treated and aged samples as shown in Figure 8(d).

Phase identification was carried out using XRD, as shown in Figure 9. XRD patterns of all four samples, *viz.*, powder, the as-printed, and solution heat-treated, and aged DMLS CoCrMo, show peaks for both the γ -FCC and ϵ -HCP Cobalt phases. Table V shows lattice parameters of both γ -FCC and ϵ -HCP phases in all samples. The volume fraction of ϵ -HCP was calculated using the Sage and Guillard^[23] equation:

$$\text{Pct hcp} = \left\{ \frac{I_{(10\bar{1}1)_{\text{hcp}}}}{I_{(10\bar{1}1)_{\text{hcp}}} + I_{(200)_{\text{fcc}}}} \right\} (100) \quad [1]$$

The calculated phase fraction of ϵ -HCP phase from the as-printed to the aged samples is given in Table VI.

Figure 10 shows the representative EBSD-IPF maps of the as-printed and solution-treated DMLS CoCrMo.

Large elongated grains can be observed in the as-printed EBSD image. These correspond to the columnar domains seen in Figure 5. The heat-treated image shows equiaxed grains with twins. There was no preferred orientation or texture in the heat-treated microstructures. Residual stress analysis was carried out on the electropolished surface of the as-printed DMLS CoCrMo. Figure 11 shows the distribution of residual stress on the surface of the sample. Residual stresses ranged between 550 and 950 MPa. It can be seen that residual stress decreases gradually along the build direction as shown in Figure 11(b). Hardness profiles were plotted along the build direction for transverse sections from different spans as shown in Figure 12(a). The hardness was found to be uniform across the DMLS coupon span without any significant difference, measuring between 420 and 460 HV. The hardness was found to decrease to 340 to 380 HV after solution heat treatment and aging, as shown in the comparative plot in Figure 12(b).

C. Tensile Properties

Figure 13 shows 0.2 pct yield strength, UTS, and ductility for the room-temperature and high-temperature (925 °C) tensile tests. The as-printed DMLS CoCrMo samples have a yield strength of ~ 1100 MPa with limited ductility (5 to 6 pct), at the room temperature. There is a 45 pct decrease in the yield strength of the solution-treated and aged sample to ~ 600 MPa, with the ductility now being enhanced to nearly 15 pct. The yield strengths of solution-treated sample and the aged sample are similar (Figure 13(a)), while the ductility decreased on aging in the room-temperature tests. The aged samples show around 70 to 80 pct decrease in both 0.2 pct yield strength and UTS, and 300 pct increase in ductility when tested at 925 °C as compared to the room-temperature tests. Figures 14(a) and (b) shows the fracture surface of the as-printed DMLS CoCrMo tested at the room temperature. Cracks and transgranular facets can be observed. Fractographs of solution-treated samples tested at the room temperature are shown Figures 14(c) and (d). Some cracks can be observed at low magnification along with dimples at higher magnification (Figure 14(c)). The fractographs of the solution-treated samples tested at high temperature (925 °C) show dimples, indicative of ductile failure (Figures 14(e) and (f)). Figures 14(g) through (j) are fractographs representative of the solution-treated and aged samples at the room temperature and at 925 °C, respectively, revealing predominantly intergranular fracture.

D. Microstructure and Tensile Strength: DMLS CoCrMo Welded to cast FSX414

Figure 15(a) is a schematic showing the welded joint between DMLS CoCrMo and cast FSX414. Figures 15(b) through (d) compares the microstructure of DMLS CoCrMo, the weld joint and cast FSX414 after the post weld heat treatment. The weldment showed a

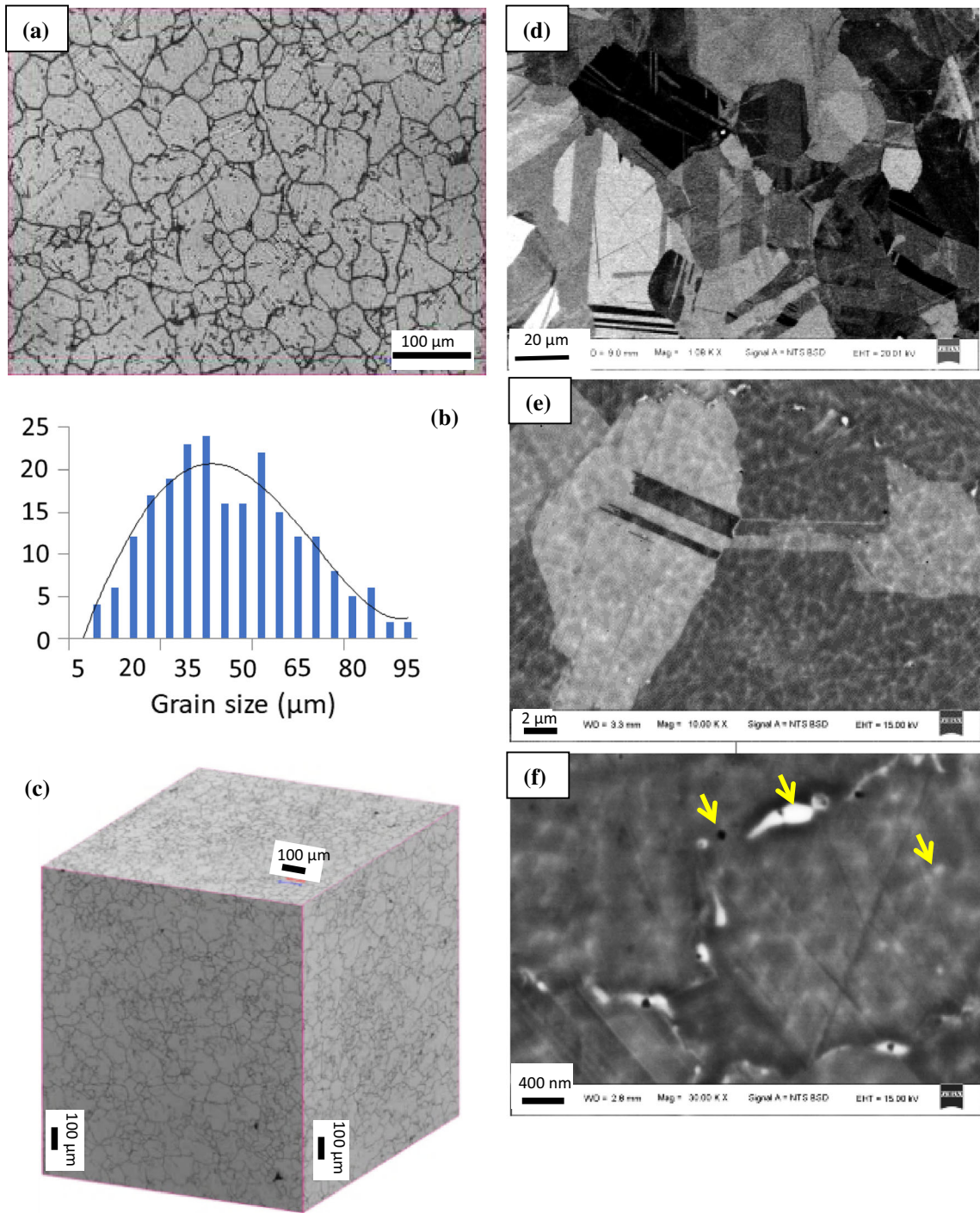


Fig. 7—Solution heat-treated DMLS CoCrMo. (a) Optical micrograph showing equiaxed microstructure with average grain size of $44\ \mu\text{m}$, (b) the corresponding grain size distribution, (c) optical micrographs of front planar and base sections, (d) BSE image showing twins, (e) along with remnants of previous interdendritic precipitates inside grains, (f) as well as precipitates along grain boundaries.

uniform microstructure, indicating a sound weld between the DMLS and cast alloy. The legends denotes pct porosity, microhardness, and grain size. The room-temperature tensile strength of the weldment was found to be 415 MPa (0.2 pct YS) and 630 MPa (UTS). The collage

of images in Figure 15(e) have been taken from a tensile test specimen after the room-temperature tensile test, indicating the location of failure to be on the side of the cast FSX414, thereby indicating that the weld joint to DMLS CoCrMo is sound.

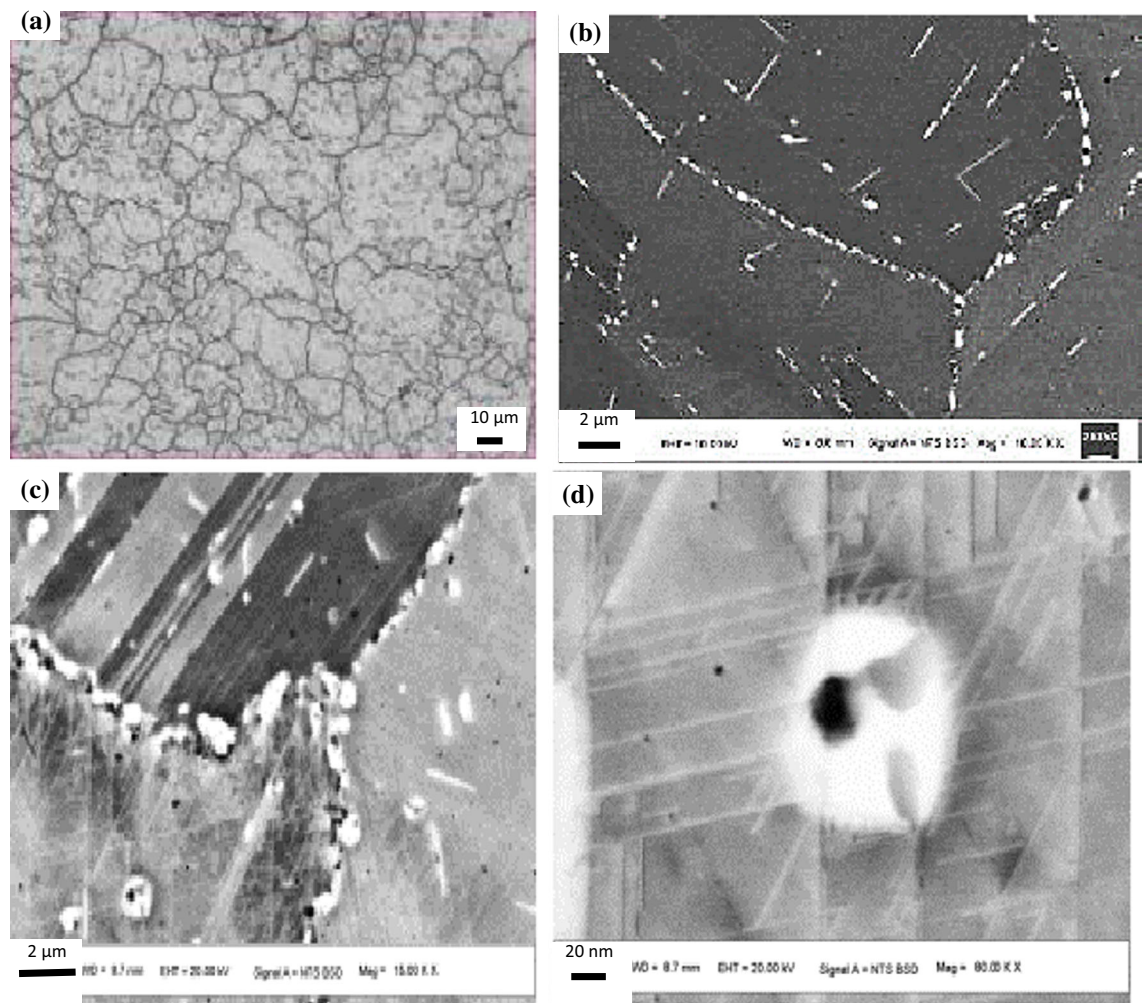


Fig. 8—(a) Optical micrographs of the solution-treated and aged DMLS CoCrMo having an equiaxed grain structure along with some precipitation, made evident *via* (b) BSE images revealing bright and dark precipitates inside the grains, (c) as well as along the grain boundaries, (d) showing ϵ -hcp, present in the matrix after aging.

Table IV. Compositions of Various Phases After Aging for DMLS CoCrMo (SEM-EDS)

Elements		Co	Cr	Mo	Mn	Si
Bright Precipitate	wt pct	51.2	27.5	17.3	1.5	2.6
	at. pct	51.1	31.2	10.7	1.6	5.5
Dark Precipitate	wt pct	47.6	38.4	10.9	2.0	1.2
	at. pct	46.5	42.5	6.5	2.1	2.4
Matrix	wt pct	63.0	28.4	6.8	0.6	0.8
	at. pct	60.9	31.1	4.07	0.6	1.6

IV. DISCUSSION

A. Microstructure of DMLS CoCrMo

The process parameters in this study were developed to ensure a nearly dense microstructure with little porosity, details of which can be found in Reference 30. Some sporadic fine pores do appear in the microstructure. The pores have a spherical and an irregular morphology. The occurrence of these fine

spherical pores can be attributed to the presence of entrapped gas within the gas atomized powders and bubbles,^[16,27] from metallic evaporation due to the high-power laser beam.^[28] Most of the irregular pores were observed along the interlayer boundaries indicative of incomplete re-melting of the previous layer. Limited microcracks that were observed are almost perpendicular to the melt pool boundary. Solidification shrinkage in the upper molten layer is restricted by the cooler substrate or previous layers, and this could be the reason behind the formation of microcracks.^[18] The molten metal pool in the DMLS process is created when the laser beam with around 80 μm diameter hits the thin CoCrMo powder layer with thickness of 40 μm . Since the size of this pool is very small ($\sim 120 \mu\text{m}$ wide and $\sim 60 \mu\text{m}$ deep), it solidifies very rapidly owing to the high rate of heat extraction from the cooler substrate/previous layers. The laser beam has maximum intensity in the center which gradually decreases toward the edge of beam due to its Gaussian energy distribution resulting in arc shaped melt pools.^[19] The laser beam scans the powder layer in a predefined path and process is

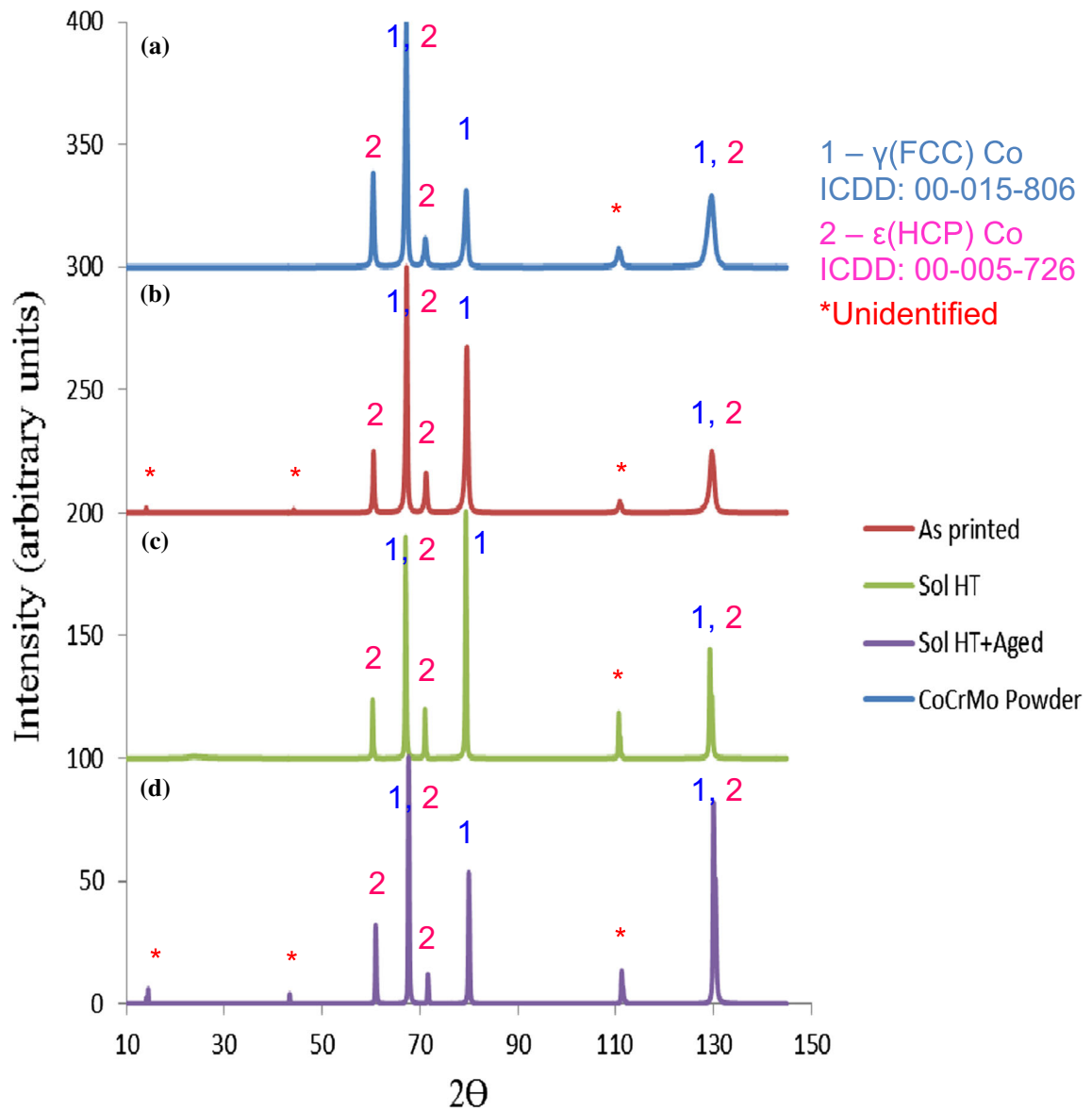


Fig. 9—X-ray diffractions patterns of (a) CoCrMo Powder, (b) the as-printed (c) Sol HT, (d) Sol HT + aged, DMLS CoCrMo, all showing peaks for both γ -FCC and ϵ -HCP Cobalt phases (Target: Cr-K α —2.29 Å).

Table V. Lattice Parameters of FCC and HCP Phases in Various CoCrMo Samples

Specimen	Lattice Parameter (Å)	
	γ -FCC	ϵ -HCP
CoCrMo Powder	$a = 3.5794$	$a = 2.5310, c = 4.7773$
As-printed DMLS CoCrMo	$a = 3.5787$	$a = 2.5305, c = 4.7742$
Sol HT DMLS CoCrMo	$a = 3.5846$	$a = 2.5347, c = 4.7867$
Sol HT + Aged DMLS CoCrMo	$a = 3.5743$	$a = 2.5274, c = 4.7493$
Pure Cobalt [source: periodictable.com]	$a = 3.5447$	$a = 2.5071, c = 4.0695$

repeated for next layers. A schematic representation of microstructural evolution during DMLS processing is shown in Figure 16. Re-melting of the previous layers as well as adjacent melt tracks is important to achieve good

bonding between them. The depth of melt pool (~ 60 μm) is higher than the powder layer thickness (40 μm) and this has ensured the above objective. The laser scanning direction is rotated by 67 deg for every

Table VI. Phase Fractions of HCP Phase in Various CoCrMo Samples

Specimen	Percent Phase Fraction of ϵ -HCP Phase
CoCrMo Powder	45.1
As-Printed DMLS CoCrMo	19.7
Sol HT DMLS CoCrMo	13.6
Sol HT + Aged DMLS CoCrMo	28.6

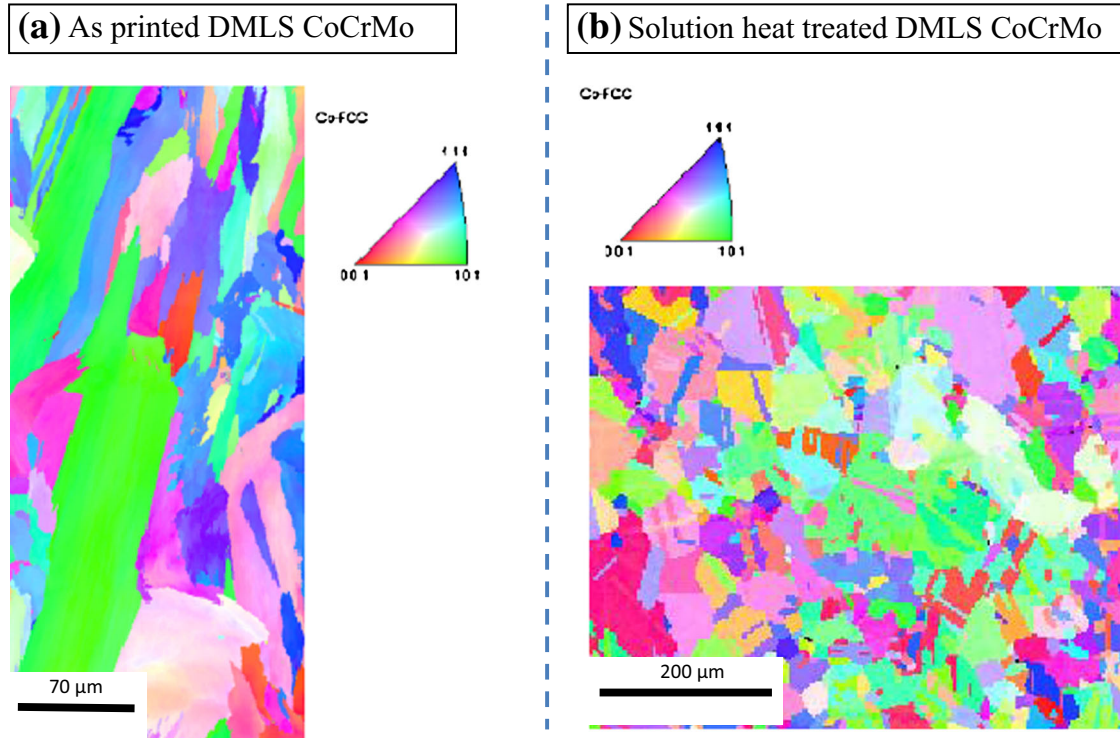


Fig. 10—EBSD IPF Maps of (a) the as-printed, (b) solution heat-treated DMLS CoCrMo.

new powder layer, as shown from the etched base microstructure in Figure 4(e). Changing scan direction decreases the residual stress accumulated during the build and minimizes the porosity in the sample and also ensures isotropy of microstructures and properties in the sample.^[29] There was no significant difference between the microstructures in the transverse and longitudinal directions. The as-printed coupon showed a uniform solidification structure throughout the coupon. The fine structure within the weld pool reveals a dendritic structure (column width of 1.5 to 2 μm) as shown in representative scanning electron micrographs in Figure 5, with molybdenum and silicon enrichment in the interdendritic regions. Takaichi *et al.*^[24] Quin *et al.*^[25] Meacock *et al.*^[29] have observed similar molybdenum and silicon rich phases in the interdendritic regions in their studies on DMLS/SLM CoCrMo. A silicon rich dark globular phase in DMLS CoCrMo was also observed by Mengucci *et al.*^[23] for DMLS CoCrMoW and Giacchi *et al.*^[26] for cast CoCrMo. Identification of elongated bright precipitate in the

interdendritic regions requires extensive TEM characterization and will be studied in greater detail in future. Mengucci *et al.*^[23] reported similar microstructural features with molybdenum and silicon enriched interdendritic precipitate for DMLS CoCrMoW alloy. The precipitate was identified as $\text{Co}_3(\text{Mo,W})_2\text{Si}$ phase with HCP crystal structure. Owing to the similar composition used in this study except the tungsten content, the most probable phase in the interdendritic region is $\text{Co}_3\text{Mo}_2\text{Si}$. TEM analysis of the as-printed DMLS CoCrMo reveals presence of ϵ -HCP martensite in the form of plates. XRD analysis also shows about 20 pct ϵ -HCP phase in the as-printed sample. Presence of athermal ϵ -HCP martensite phase and its formation mechanism in CoCrMo alloy is widely reported in literature^[19–21,27,28] for DMLS CoCrMoW alloy. TEM analysis of the as-printed DMLS CoCrMo reveals presence of ϵ -HCP martensite in the form of plates. ϵ -HCP phases grow on $\{111\}$ planes of γ -FCC matrix. Since $\{111\}$ planes parallel to the electron beam direction are at 70 deg angle for $[011]$ zone axis, ϵ -HCP plates can be observed

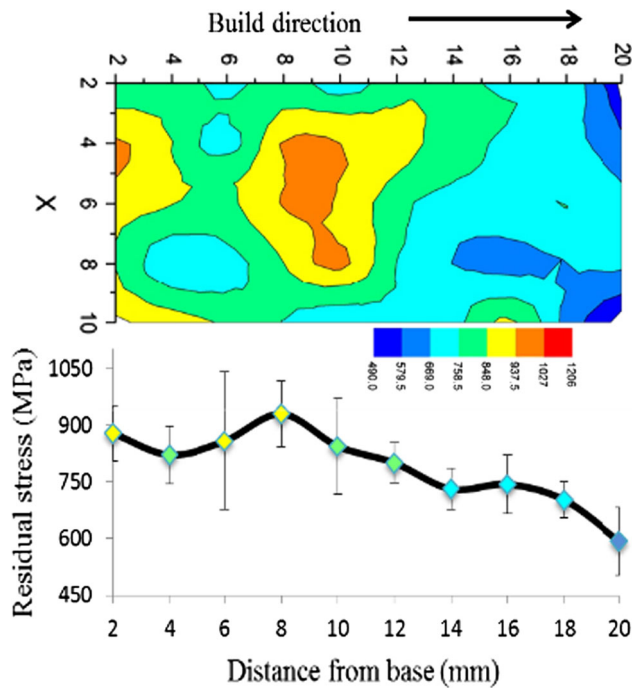


Fig. 11—Residual stress distribution on the surface of the as-printed DMLS CoCrMo, measured along the build direction.

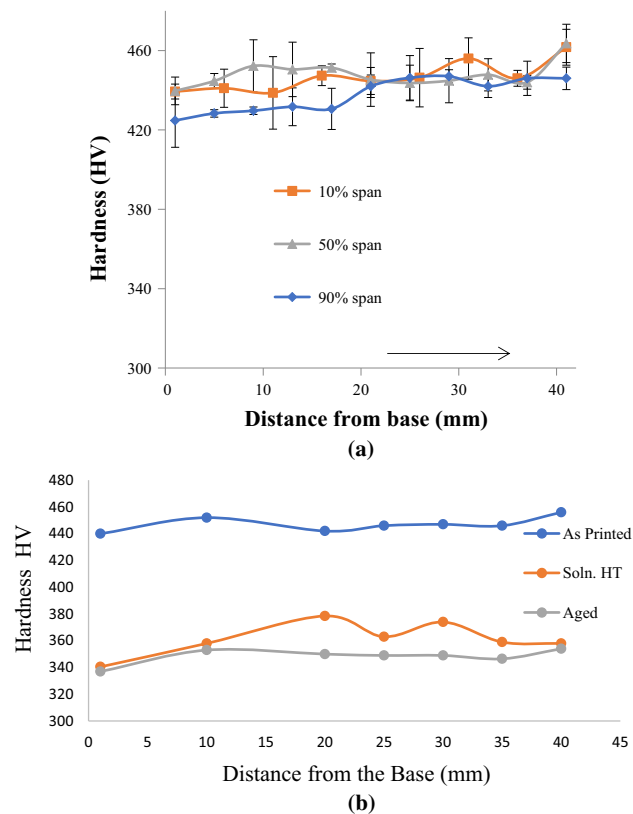


Fig. 12—(a) Hardness profile along build direction in the as-printed DMLS CoCrMo, (b) comparison of hardnesses across the 50 pct span in the as-printed, solution-treated, and the solution and aged conditions.

with same angle between them as shown in Figure 6. In addition, plates on other $\{111\}$ planes are inclined to the electron beam direction and show fringe contrast in Figure 6. In pure cobalt, the FCC to HCP transformation is around 417°C . The transformation temperature can increase in the presence HCP stabilizer elements like Cr, Mo, Si, *etc.* Because of the sluggish kinetics of the FCC-HCP transformation, the transformation to ϵ -HCP Co is limited.

The microstructure of the solution heat-treated sample is fully equiaxed. Table VII lists a comparison of size and morphology of grains in the as-printed, solution-treated and aged DMLS CoCrMo. Solution heat treatment results in breakdown of columnar dendritic domains into equiaxed grains, a process that is probably driven by the residual stress present in the sample as shown in the schematic in Figure 17. The average microhardness of the as-printed CoCrMo was ~ 444 HV, which is nearly 1.5 times that of the cast-CoCrMo (250 to 350 HV).^[21] The high hardness in the as-printed condition is attributed to a combination of, the fine columnar structure with an interdendritic phase (*via* a Hall-Petch-type strengthening) and the residual stress generated during DMLS processing (which has been measured to range to as high as 950 MPa, in this study). Upon heat treatment, the DMLS coupon is seen to undergo recrystallization to result in a uniform equiaxed structure, having an average grain size of 40 to 50 μm , as shown in Figure 7. The heat-treated structure shows annealing twins, characteristic of a low stacking fault energy material. The microhardness of the heat-treated DMLS CoCrMo is ~ 350 HV. Preliminary phase identification using X-ray diffraction revealed both γ (FCC) and ϵ (HCP) phases, as shown in a comparative plot in Figures 9(a) through (d). A distinct peak broadening is observed in the as-printed condition as compared to the heat-treated one, in both the phases. The sharpening of peaks upon heat treatment is attributed to a relieving of residual stress.

Table VIII shows the size, location, and morphology of various precipitates in the as-printed, solution heat-treated and aged DMLS CoCrMo. The bright precipitate in solution-treated sample (Figure 7) is due to the remnants of the prior interdendritic region, indicating incomplete homogenization. Few globular bright precipitates can also be observed along the grain boundaries. The size of these precipitates is around 235 nm, which is higher than the width of interdendritic precipitates from the as-printed structure (~ 80 nm), as shown in Table VIII. The globular dark precipitates in the solution-treated samples are the silicon rich inclusions from the as-printed samples. Microstructures of the solution-treated and aged samples show bright and dark precipitates present along the entire grain boundary. The precipitates along the grain boundary are very similar to those observed in solution heat-treated sample except that they are coarser. In addition, aging treatment has resulted in more bright precipitates along the grain boundary (globular) as well as inside grains

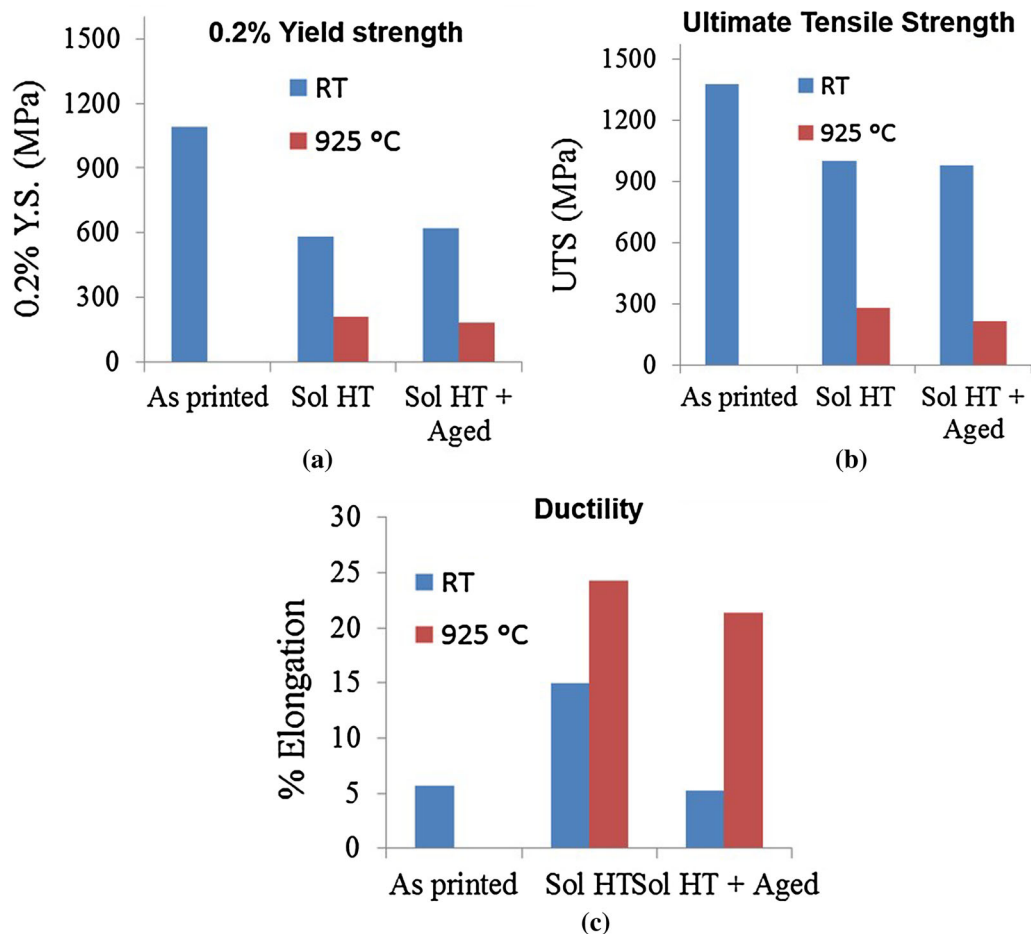


Fig. 13—(a) Room-temperature and high-temperature tensile properties of the as-printed, solution-treated, and aged, DMLS CoCrMo. (a) pct Y.S., (b) UTS, (c) ductility.

(plate-like). The plate-like bright precipitates can be observed predominantly along the twin boundaries and ϵ -HCP plates as shown in Figure 8. Both grain boundary bright precipitates and plate-like precipitates inside grains are molybdenum and silicon rich as shown in Table IV. Figure 18(a) shows isothermal section of the CoCrMo ternary phase diagram at 1200 °C. The current alloy composition is exactly at the boundary between γ and σ ($\text{Co}_9\text{Mo}_{15}$) phase. Thus, it is expected that these samples will have a certain amount of σ phase after solution treatment at 1150 °C. The isothermal section of the CoCrMo ternary phase diagram at 924 °C (Figure 18(b)) also shows the presence of ϵ and σ phase. XRD analysis shows the increasing volume fraction of ϵ -HCP after aging at 980 °C as compared to the solution-treated DMLS CoCrMo, as shown in Table VI. The molybdenum and silicon rich precipitates in the solution-treated and aged DMLS CoCrMo have a very similar chemistry to the interdendritic precipitates. Thus, although the ternary phase diagram predicts the presence of σ -phase in the heat-treated samples, the presence of silicon is likely to have shifted the equilibria toward that of interdendritic precipitate (probably $\text{Co}_3\text{Mo}_2\text{Si}$). Identification of precipitates in the

as-printed and heat-treated DMLS CoCrMo requires extensive TEM characterization, which will be reported in the future.

B. Tensile Properties of Direct Metal Laser-Sintered (DMLS) CoCrMo

The as-printed samples show the highest yield stress. The yield stress decreases considerably after solution heat treatment and remains unaffected after aging. The decrease in strength reflects the breakdown of the fine scale columnar structure (~ 800 nm in width) with an extremely fine primary dendrite arm spacing in the as-printed material to the ~ 40 μm equiaxed grain size in solution heat-treated material that emerges from the columnar domains of the as-printed structure. After aging there is almost no change in the grain size. However, the extensive precipitation along the grain boundaries as well as inside grains does not seem to play any role in increasing the strength of the alloy. Fractographs of the as-printed samples showing facets and secondary cracks indicate cleavage type fracture. Thus, the as-printed samples have a brittle failure mode at the room temperature and is associated with low ductility.

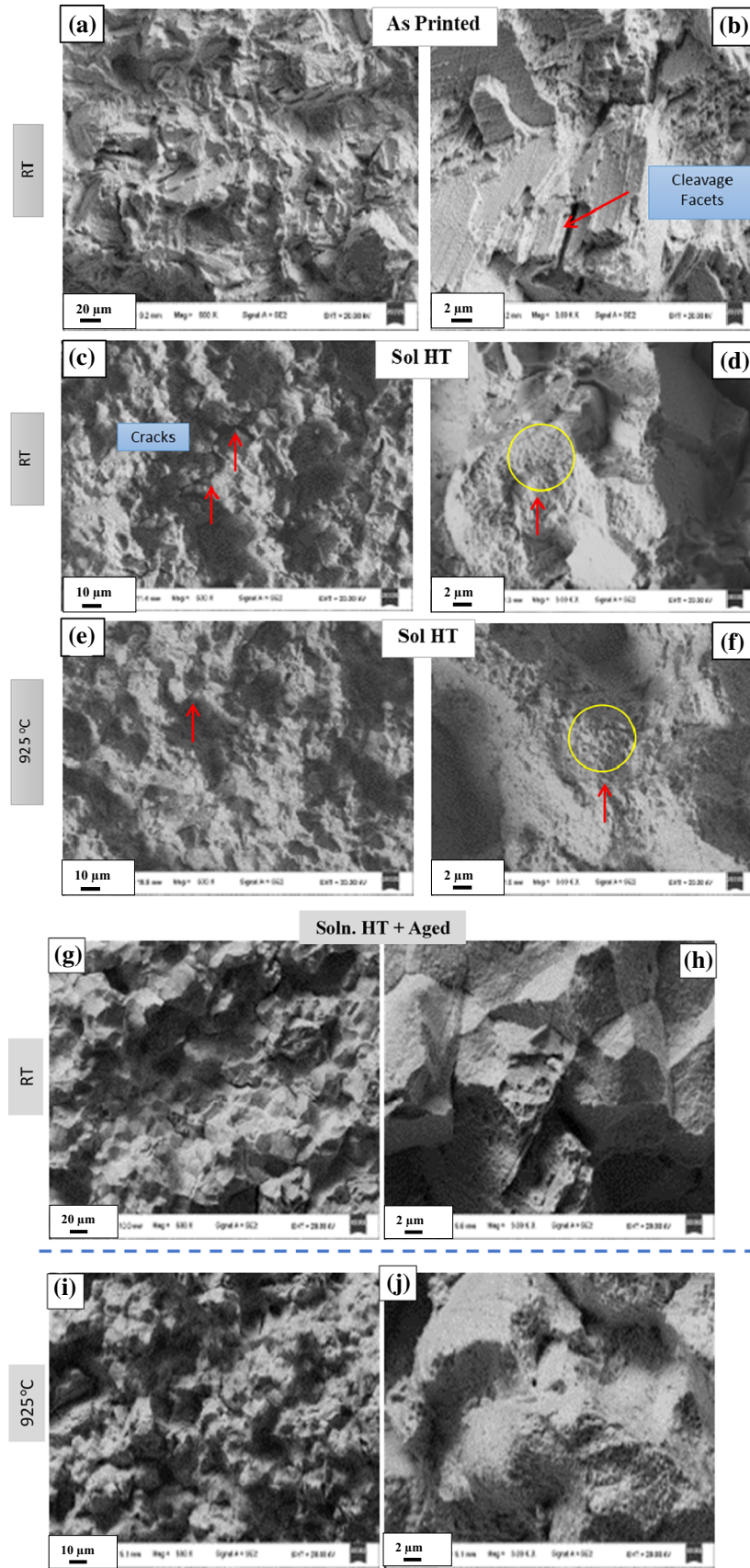


Fig. 14—Fractographs of DMLS CoCrMo, (a, b) the as-printed showing cracks and facets at the room temperature, solution-treated condition having mixed brittle and ductile type failures, (c, d) at the room temperature, (e, f) at 925 °C. Fractographs of solution-treated and aged DMLS CoCrMo, showing intergranular fracture at (g, h) room temperature and (i, j) at 925 °C.

Figure 19 shows schematic representation of engineering stress vs engineering strain curve for the room-temperature-tested, the as-printed, and solution-treated DMLS CoCrMo. The very high UTS of the as-printed sample as compared to cleavage stress of CoCrMo may be the reason for its brittle failure mode. Solution-treated samples show relatively higher ductility in the room-temperature tensile tests. The presence of

intergranular cracks and dimples in the fractographs of the room-temperature-tested samples reveal mixed ductile and brittle failure modes. It appears that the decrease in yield stress associated with the larger recrystallised grain structure and the relief of residual stress allows plasticity to develop before fracture intervenes. The aged samples (in the room-temperature tests) show considerably lower ductility values than solution

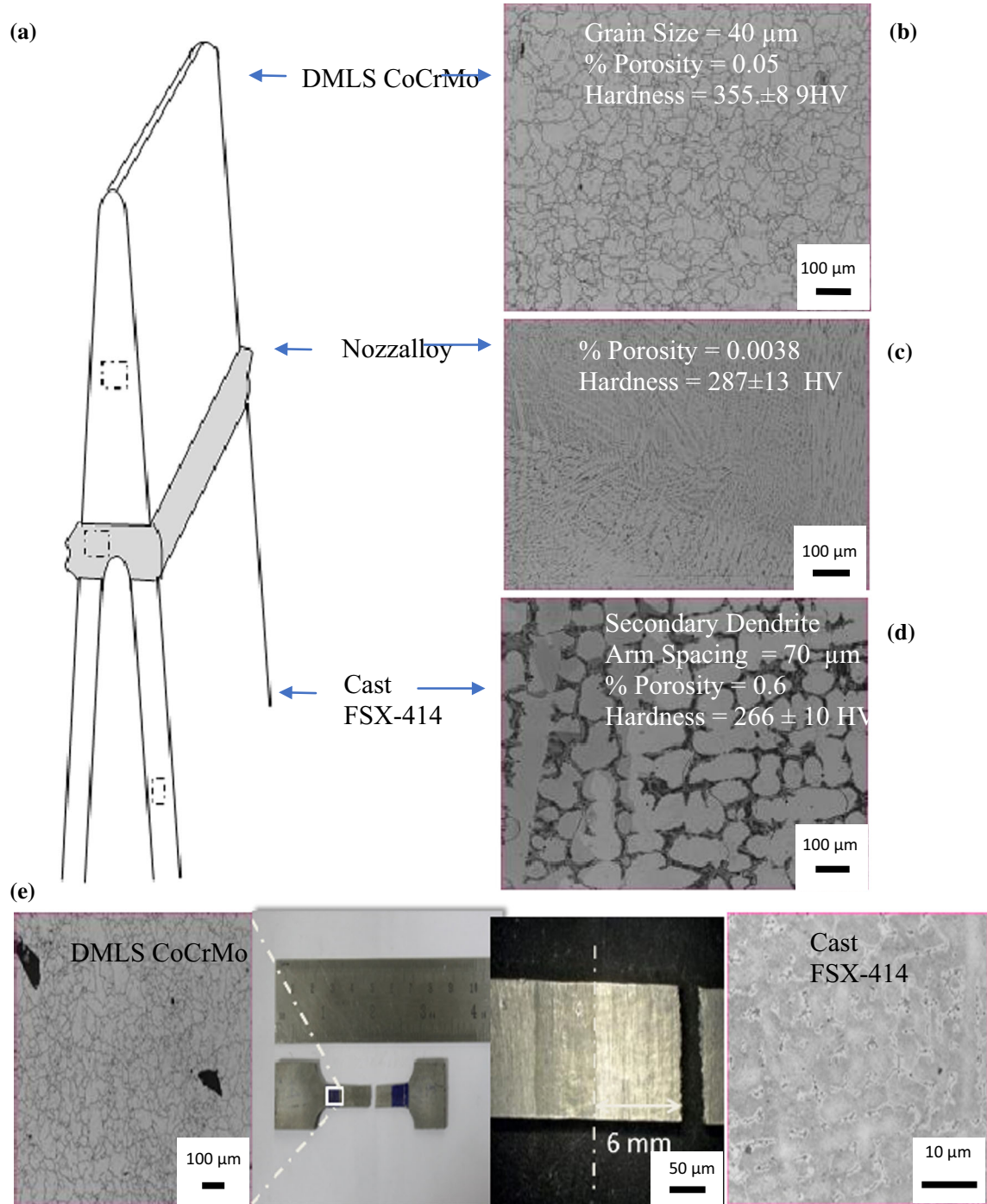


Fig. 15—(a) Schematic of the welded joint between DMLS CoCrMo and cast FSX414; (b, d) representative optical micrographs from DMLS CoCrMo, Nozzle alloy filler wire, and cast FSX414 after postweld heat treatment, with legends displaying the grain size, porosity, and hardness. (e) Collage of images taken from the tensile-tested specimen revealing the failure to take place in the cast FSX414.

heat-treated samples. Fractographs shows cracks and reveals mainly intergranular brittle fracture. This can be attributed to the intergranular precipitate phases, which supports propagation of intergranular cracks. Low 0.2 pct Y.S. and UTS at high-temperature tests are mainly because thermally activated mechanisms assist

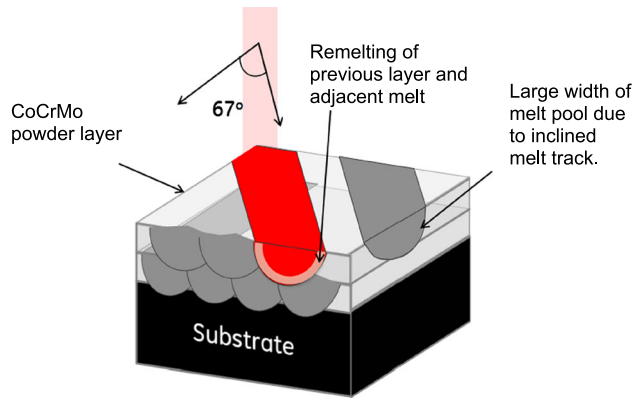


Fig. 16—Schematic representation of microstructural evolution in DMLS CoCrMo.

deformation and decrease strength of the material.^[31] In many FCC materials, UTS is more temperature dependent than 0.2 pct Y.S.^[31] Both strength (0.2 pct Y.S., UTS) and ductility are almost similar for high-temperature-tested solution and aged samples. A mixed ductile and brittle mode can be observed in the fractographs of both high-temperature-tested solution heat-treated and Sol HT + Aged samples. The grain boundary precipitates so not result in a lower ductility in high-temperature tensile tests. Finally, DMLS CoCrMo was successfully welded to cast FSX414 with the weldment showing a uniform microstructure, indicating a sound weld between the DMLS and cast alloys. The tensile properties of the weld were superior to that of the cast FSX414 thereby bringing out the suitability of a DMLS part for practical applications.

V. CONCLUSIONS

This study presents the detailed microstructural characteristics of DMLS CoCrMo in the as-printed and heat-treated and aged conditions. A dense structure was produced in the as-printed condition, without having to

Table VII. Sizes and Morphologies of Grains in As-Printed, Solution-Treated and Aged DMLS CoCrMo

Treatment	Grain Morphology	Grain/Domain Size (μm)	
		Range (μm)	Average Value (μm)
As-Printed	elongated	10 to 70	~ 39
	width	40 to 290	~ 104
	length	5 to 90	~ 44
Sol HT	equiaxed	5 to 90	~ 43
Sol HT + Aged	equiaxed	5 to 90	~ 43

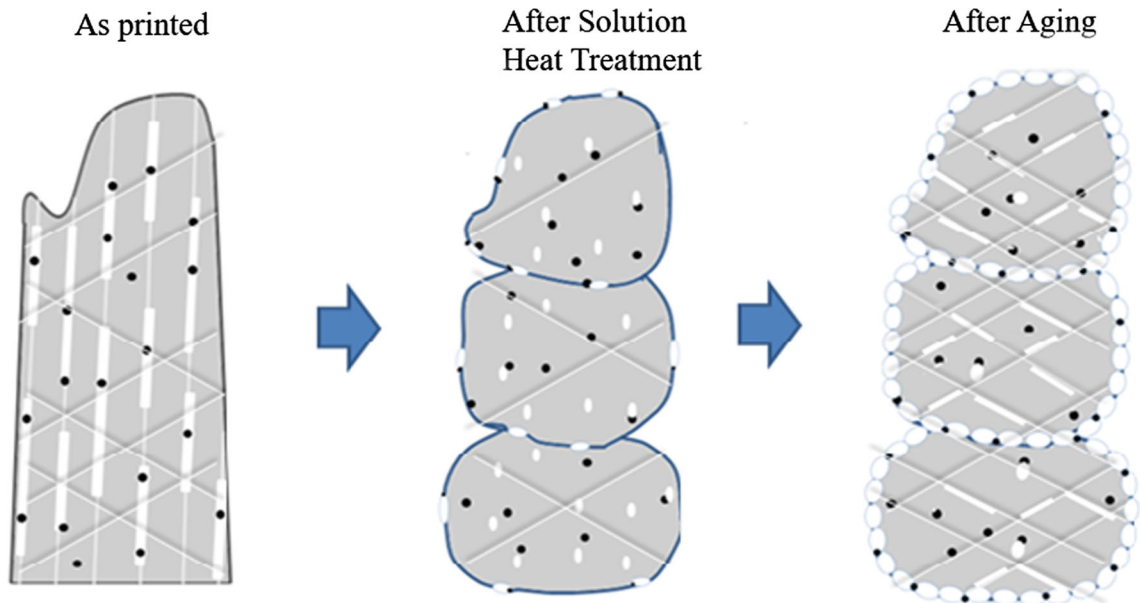


Fig. 17—Schematic representation of microstructural changes during solution and aging heat treatments.

Table VIII. Size and Morphology of Precipitates Observed in the As-Printed, Solution-Treated, and Aged DMLS CoCrMo

Treatment	Morphology and Contrast	Location	Precipitate Size		
			(nm)	Range (nm)	Average (nm)
As-Printed	elongated bright globular dark	interdendritic region everywhere	width diameter	50 to 105 15 to 100	~ 80 ~ 35
Sol HT	globular/elliptical bright globular dark	grain boundary everywhere	diameter diameter	100 to 400 40 to 160	~ 235 ~ 86
Sol HT + Aged	globular/elliptical bright plate bright	predominantly along grain boundary, some inside grains inside grains—along twin boundaries and ϵ -plates	diameter width	175 to 725 70 to 120	~ 390 ~ 95
	globular dark	everywhere	length diameter	1000 to 3000 26 to 325	~ 1480 ~ 160

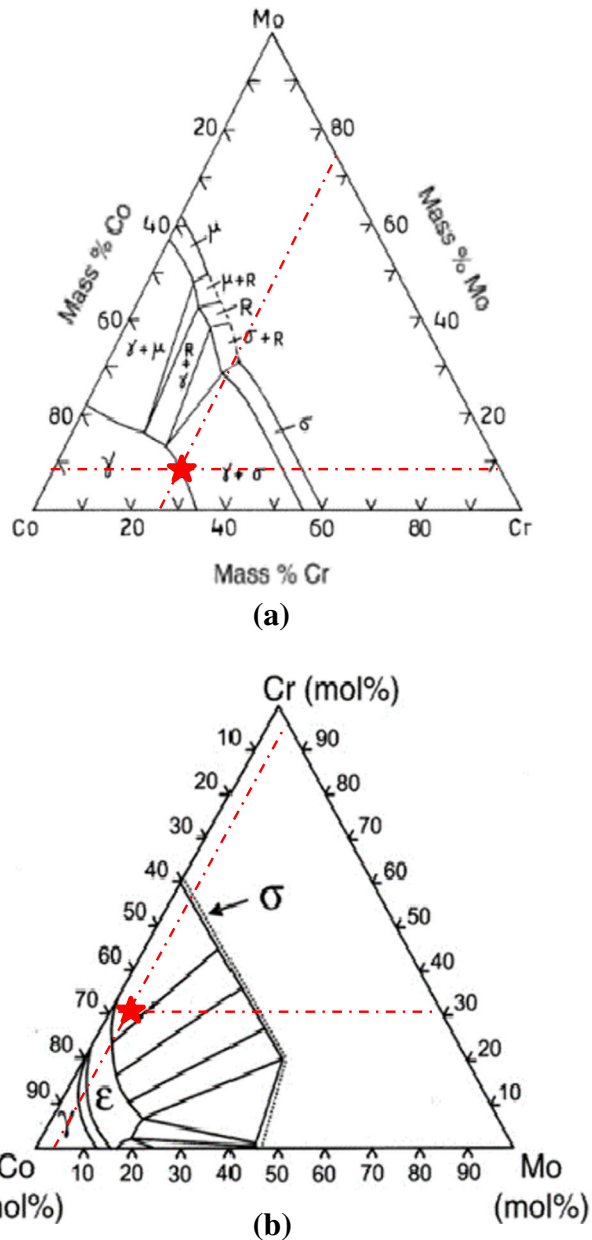


Fig. 18—Isothermal sections of CoCrMo ternary diagram at (a) 1200 °C, (b) 924 °C.

undergo HIP treatment. The microstructure inside the melt pool shows very fine columnar, dendritic structure with the Mo and Si segregation in the interdendritic regions. Columns with same orientation are seen growing across the melt pool boundaries and forming elongated domains/grains, with athermal ϵ -HCP martensite which forms due to rapid solidification. Heat treatment results in an equiaxed grain structure ($\sim 40 \mu\text{m}$) as a result of the breakdown of the elongated grains *via* recrystallization. The thermal response of the DMLS CoCrMo is *via* precipitation of Mo- and Si-enriched phases both within the grains and along the grain boundaries. Hardness and tensile strength remain the same after aging treatment. The

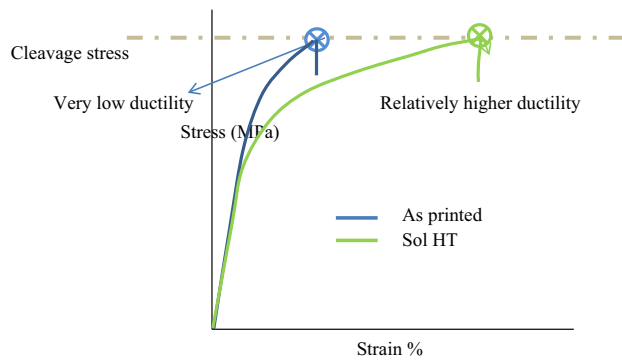


Fig. 19—Schematic representation of engineering stress vs engineering strain curve for the as-printed and solution-treated DMLS CoCrMo (room temperature).

intergranular failure seen with very low ductility after aging can be attributed to extensive precipitation along the grain boundaries. The study was able to successfully demonstrate the welding of the DMLS CoCrMo to a cast FSX414 without any deterioration in the weld joint.

ACKNOWLEDGMENTS

This study was done during the internship tenure of Kaustubh Krishna Bawane at the Repair Development Center, GE Power, Bangalore, India. The authors are thankful to the manager, Christopher Thompson, at the Repair Development Center, GE Power for funding this study. M. Raghunandan and S. Rohith of Intech DMLS Pvt. Ltd, Bangalore, are gratefully thanked for providing the DMLS CoCrMo coupons for this study. The welding trials were carried out with the help of Mohammed Anwar, Gulf Turbine Services (GTS), Abu Dhabi. The authors are grateful to Abhik Narayan Choudhury (IISc, Bangalore), Dayananda Narayana and Joydeep Pal (GE Power, Bangalore), and Mariusz Strzyszewski (GE Power, Poland), for various fruitful discussions during the course of this study. S. Sashidhara and Vinay Kunnathulli of the Materials Engineering department, IISc, Bangalore, are thanked for their help in carrying out the micro-tensile testing and the TEM characterization.

REFERENCES

1. T. Wohlers and T. Gornet: *Wohlers Rep.*, 2014, vol. 2014, pp. 1–23.
2. R. A. of Engineering, *R. Acad. Eng.*, 2013, pp. 21–31.
3. F.H. Froes and B. Dutta: *Adv. Mater. Res.*, 2014, vol. 1019, pp. 19–25.
4. T. Grunberger and R. Domrose: *Laser Techn. J.*, 2015, vol. 12, pp. 45–48.
5. C.E. Santos, M. Shiomi, and K. Osakada: *Int. J. Mach. Tools Manuf.*, 2006, vol. 46, pp. 1459–68.
6. F. Abe, K. Osakada, M. Shiomi, and M. Matsumoto: *J. Mater. Process. Technol.*, 2001, vol. 111, pp. 210–13.
7. P.L. Blackwell and A. Wisbey: *J. Mater. Process. Technol.*, 2005, vol. 170, pp. 268–76.
8. J. Alcisto, A. Enriquez, H. Garcia, S. Hinkson, T. Steelman, E. Silverman, P. Valdovino, H. Gigerenzer, J. Foyos, J. Ogren, J. Dorey, K. Karg, T. McDonald, and O.S. Es-Said: *J. Mater. Eng. Perform.*, 2011, vol. 20, pp. 203–12.
9. W.E. Frazier: *J. Mater. Eng. Perform.*, 2014, vol. 23, pp. 1917–28.
10. P. Kanagarajah, F. Brenne, T. Niendorf, and H.J. Maier: *Mater. Sci. Eng. A*, 2013, vol. 588, pp. 188–95.
11. K.N. Amato, S.M. Gaytan, L.E. Murr, E. Martinez, P.W. Shindo, J. Hernandez, S. Collins, and F. Medina: *Acta Mater.*, 2012, vol. 60, pp. 2229–39.
12. L. Rickenbacher, T. Etter, S. Hövel, and K. Wegener: *Rapid Prototyp. J.*, 2013, vol. 19, pp. 282–90.
13. Q. Jia and D. Gu: *J. Alloys Compd.*, 2014, vol. 585, pp. 713–21.
14. P. Nie, O.A. Ojo, and Z. Li: *Acta Mater.*, 2014, vol. 77, pp. 85–95.
15. T. Vilaro, C. Colin, J.D. Bartout, L. Nazé, and M. Sennour: *Mater. Sci. Eng. A*, 2012, vol. 534, pp. 446–51.
16. H. Gong, K. Rafi, H. Gu, T. Starr, and B. Stucker: *Addit. Manuf.*, 2014, vol. 1, pp. 87–98.
17. A. Bauereiß, T. Scharowsky, and C. Körner: *J. Mater. Process. Technol.*, 2014, vol. 214, pp. 2522–28.
18. N.J. Harrison, I. Todd, and K. Mumtaz: *Acta Mater.*, 2015, vol. 94, pp. 59–68.
19. C. Yan, L. Hao, A. Hussein, P. Young, J. Huang, and W. Zhu: *Mater. Sci. Eng. A*, 2015, vol. 628, pp. 238–46.
20. Cobalt Facts, “Cobalt in Metallurgical Uses,” *Cobalt Facts*, 2006, pp. 8–22.
21. G. Barucca, E. Santecchia, G. Majni, E. Girardin, E. Bassoli, L. Denti, A. Gatto, L. Iuliano, T. Moskalewicz, and P. Mengucci: *Mater. Sci. Eng.*, 2015, vol. 48, pp. 263–69.
22. T. Takashima, Y. Koizumi, Y. Li, K. Yamanaka, T. Saito, and A. Chiba: *Mater. Trans.*, 2015, vol. 57, pp. 305–18.
23. P. Mengucci, G. Barucca, A. Gatto, E. Bassoli, L. Denti, F. Fiori, E. Girardin, P. Bastianoni, B. Rutkowski, and A. Czyska-Filemonowicz: *J. Mech. Behav. Biomed. Mater.*, 2016, vol. 60, pp. 106–17.
24. A. Takaichi, T. Nakamoto, N. Joko, N. Nomura, Y. Tsutsumi, S. Migita, H. Doi, S. Kurosu, A. Chiba, and N. Wakabayashi: *J. Mech. Behav. Biomed. Mater.*, 2013, vol. 21, pp. 67–76.
25. B. Qian, K. Saeidi, L. Kvetková, F. Lofaj, C. Xiao, and Z. Shen: *Dent. Mater.*, 2015, vol. 31, pp. 1435–44.
26. J.V. Giacchi, C.N. Morando, O. Fornaro, and H.A. Palacio: *Mater. Charact.*, 2011, vol. 62, pp. 53–61.
27. D.J. Saldívar García, M. Medrano, and S. Rodríguez: *Metall. Mater. Trans. A*, 1999, vol. 30A, pp. 1177–84.
28. X. Zhou, D. Wang, X. Liu, D. Zhang, S. Qu, J. Ma, G. London, Z. Shen, and W. Liu: *Acta Mater.*, 2015, vol. 98, pp. 1–16.
29. C.G. Meacock and R. Vilar: *J. Laser Appl.*, 2009, vol. 21 (2), pp. 88–95.
30. S.K. Rao Chandrasekara, A.S. Reddy, D. Srinivasan, and D. Ananthanarayanan: Proceedings of the ASME 2017 Gas Turbine India Conference GTINDIA2017-4614, December 2017.
31. H. Fujita and S. Ueda: *Acta Metall.*, 1972, vol. 20, pp. 657–767.